

Temperature-field phase diagram of extreme magnetoresistance in lanthanum monopnictides

F. F. Tafti,^{1,*} Q. D. Gibson,¹ S. K. Kushwaha,¹ J. W. Krizan,¹ N. Haldolaarachchige,¹ and R. J. Cava¹

¹*Princeton University, Chemistry department, Princeton, New Jersey, USA*

(Dated: October 21, 2018)

The recent discovery of extreme magnetoresistance in LaSb introduced lanthanum monopnictides as a new platform to study topological semimetals (TSMs). In this work we report the discovery of extreme magnetoresistance in LaBi confirming lanthanum monopnictides as a promising family of TSMs. These binary compounds with the simple rock-salt structure are ideal model systems to search for the origin of extreme magnetoresistance. Through a comparative study of magnetotransport effects in LaBi and LaSb, we construct a *triangular* temperature-field phase diagram that illustrates how a magnetic field tunes the electronic behavior in these materials. We show that the triangular phase diagram can be generalized to other topological semimetals with different crystal structures and different chemical compositions. By comparing our experimental results to band structure calculations, we suggest that extreme magnetoresistance in LaBi and LaSb originates from a particular orbital texture on their quasi-2D Fermi surfaces. The orbital texture, driven by spin-orbit coupling, is likely to be a generic feature of various topological semimetals.

PACS numbers: 75.47.-m, 71.70.Ej, 71.30.+h, 71.18.+y

I. INTRODUCTION

Materials with large magnetoresistance (MR) have applications in electronics as magnetic memories [1, 2], in spintronics as magnetic valves [3], and in industry as magnetic sensors or magnetic switches [4, 5]. The magnitude of MR is determined by the ratio $R(H)/R(0)$ where R is the electrical resistance and H is the magnetic field. This ratio is large either when the numerator $R(H)$ is large or when the denominator $R(0)$ is small. A large numerator is responsible for the well-known Giant and Colossal Magnetoresistance (GMR and CMR) in magnetic semiconductors [2, 6]. A small denominator is responsible for the recently-found extreme magnetoresistance (XMR) in Dirac semimetals (DSMs) such as Na_3Bi or Cd_3As_2 [7, 8], in Weyl semimetals (WSMs) such as NbP, NbAs, or TaAs [9–11], and in layered semimetals (LSMs) such as WTe_2 , NbSb_2 , or PtSn_4 [12–16]. DSMs are characterized by strictly linear band crossing at the Dirac point. [17]. WSMs are characterized by noncentrosymmetric structures, Fermi arcs, and chiral anomaly [7, 18, 19]. LSMs are characterized by nearly perfect compensation between electron and hole bands [12, 15, 20]. The recent discovery of XMR in LaSb that lacks strictly linear band crossing, non-centrosymmetric structure, chiral anomaly, and perfect compensation shows that none of these factors control XMR. This work presents a systematic study to understand the origin of XMR.

We report the discovery of XMR in LaBi with similar crystal structure and chemical composition to LaSb. A recent theoretical work has pointed out that the simple NaCl-type structure of lanthanum monopnictides (Fig. 1) makes them ideal model systems to study the properties of topological semimetals [21]. Through a comparative study of longitudinal and transverse magnetotransport effects in the two related materials, LaSb and LaBi, we construct a *triangular* T - H phase diagram for XMR

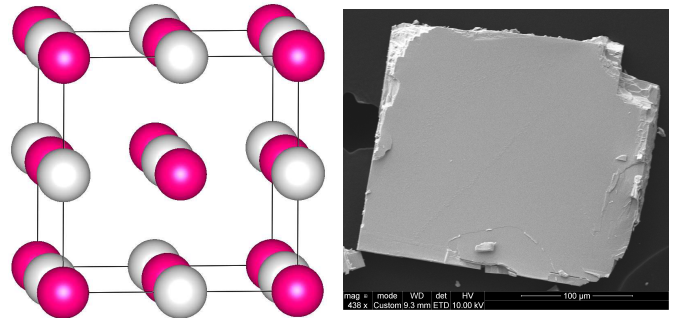


FIG. 1. (left) NaCl-type crystal structure of LaSb/LaBi with space group $Fm\bar{3}m$. Gray spheres represent La and pink spheres represent Sb/Bi. (right) Environmental Scanning Electron Microscopy (ESEM) image of a single crystal of LaBi showing its cubic symmetry and the cleaved [100] surface of the crystal. X-ray patterns and structural refinements are presented in Appendix A.

in lanthanum monopnictides. From band structure calculations, quantum oscillations, and Hall Effect measurements, we suggest that XMR is rooted in a d - p orbital mixing on the quasi-2D electron pockets that dominate the low temperature electrical transport in lanthanum monopnictides. Further, we show that similar quasi-2D Fermi surfaces with mixed orbital content exist in other TSMs and so does the triangular T - H phase diagram. These results provide compelling evidence for XMR being rooted in quasi-2D Fermi surfaces with mixed d - p orbital texture.

II. METHODS

Single crystals of LaBi were grown using Indium flux. The starting elements La:Bi:In = 1:1:20 with purity

99.999% were placed in an alumina crucible inside an evacuated quartz tube. The mixture was heated to 1000 C, slowly cooled to 700 C, and finally decanted in a centrifuge. Similar procedure was used to grow single crystals of LaSb from tin flux [22]. Energy dispersive x-ray spectroscopy (EDX) on each sample confirmed a 1:1 ratio of lanthanum to pnictogen with $\pm 1\%$ error. X-ray diffraction (XRD) patterns of both materials are presented in Appendix A.

Measurements were performed on two samples: one single crystal of LaSb with residual resistivity $\rho_0 = 0.6 \mu\Omega\text{cm}$ and residual resistivity ratio $\text{RRR} = \rho(300\text{K})/\rho_0 = 170$ and one single crystal of LaBi with $\rho_0 = 0.1 \mu\Omega\text{cm}$ and $\text{RRR} = 610$. The resistivity measurements were performed in a Quantum Design PPMS using a standard four probe method. Hall voltages were measured with transverse contacts in negative and positive fields with the data antisymmetrized to calculate the transverse resistivity ρ_{xy} and the Hall coefficient $R_H = \rho_{xy}/H$.

III. RESULTS

A. Temperature dependence of resistivity

Fig. 2(a) and 2(b) show the temperature dependence of resistivity in LaSb and LaBi. In both systems, with decreasing temperature, resistivity decreases initially until a minimum at T_m , then increases until an inflection at T_i where it gradually saturates to a plateau. Fig. 2(c) is a plot of $\partial\rho/\partial T$ versus T for LaBi which marks T_m as the sign change temperature and T_i as the peak temperature. With increasing field, T_m increases but T_i remains unchanged. Fig. 2(d) is an Arrhenius plot of $\log(\rho)$ versus T^{-1} for LaBi. It shows that between T_m and T_i the material behaves like semiconductors with $\rho(T) \propto \exp(E_a/k_B T)$ where E_a is an activation energy and k_B is the Boltzmann constant. The activation energy at each field corresponds to the slope of the linear fits in Fig. 2(d). The LaSb versions of Figs. 2(c) and 2(d) are presented in Ref. [22].

Inset of Fig. 2(b) shows that the resistivity activation in LaBi is absent at zero field; it is switched on with a small magnetic field $H_{\text{onset}} = 0.4 \pm 0.1 \text{ T}$ similar to LaSb [22]. Both materials have potential application as low temperature magnetic switches. Below T_m , $\rho(T)$ in LaSb and LaBi is analogous to $\rho(T)$ in topological insulators (TIs) such as $\text{Bi}_2\text{Te}_2\text{Se}$ and SmB_6 . In TIs the resistivity activation comes from an insulating bulk, and the plateau from conducting surface states [23–26]. In LaSb and LaBi, a similar activation and plateau appear only when time reversal symmetry is broken by a small magnetic field. In section III D, we show that the conduction in the plateau region of these materials is dominated by quasi-2D bulk states in analogy to the strictly 2D surface states of TIs.

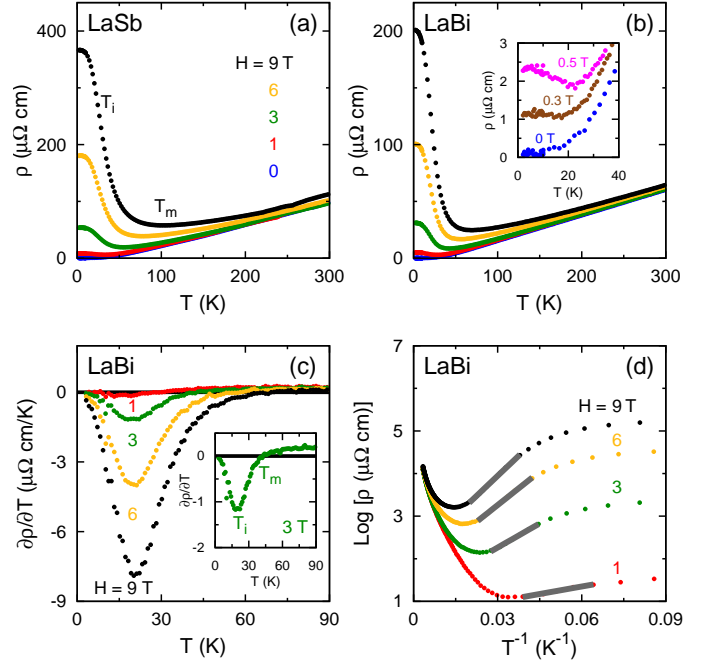


FIG. 2. (a) Resistivity as a function of temperature in LaSb at several magnetic fields as indicated on the figure. Temperature of resistivity minimum T_m and inflection T_i are marked on the black curve at $H = 9 \text{ T}$. (b) $\rho(T)$ in LaBi at the same fields as in LaSb. Inset shows $\rho(T)$ at low T and low H to capture the onset of resistivity activation at $H_{\text{onset}} = 0.4 \pm 0.1 \text{ T}$. (c) $\partial\rho/\partial T$ as a function of temperature in several fields as indicated on the figure for LaBi. Inset shows the sign change temperature T_m and the peak temperature T_i for the green curve at $H = 3 \text{ T}$. (d) Arrhenius plot of $\log(\rho)$ versus T^{-1} used to extract the activation energy E_a at several fields as indicated on the figure for LaBi.

B. Phase Diagram

By plotting T_m and T_i as a function of magnetic field, we construct the temperature-field phase diagram of LaSb and LaBi in Fig. 3(a) and 3(b). In both systems, T_m increases with increasing field while T_i stays unchanged. The shaded triangle between T_m and T_i marks the region of activated resistivity. Fig. 3(c) and 3(d) show that the activation energy E_a starts from zero at H_{onset} and increases with a non-monotonic field dependence. E_a at each field is extracted from the Arrhenius analysis explained in section III A and Fig. 2(d). Notably E_a is comparable in both systems and scales only with the magnetic field showing that the resistivity activation is controlled entirely by the magnetic field.

The triangular phase diagrams in Figs. 3(a) and 3(b) highlight three distinct resistivity behaviors in Figs. 2(a) and 2(b). The shaded triangle is the region of activated resistivity with semiconducting behavior. In the silver region above the triangle ($T > T_m$) the semiconducting behavior is replaced with the metallic conduction. In the gold region below the triangle ($T < T_m$) the semi-

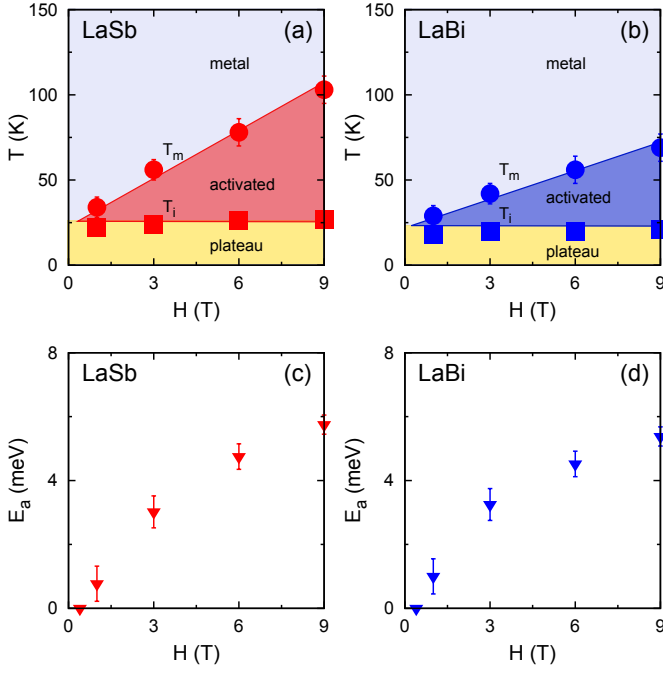


FIG. 3. (a) T_m (circles) and T_i (squares) plotted as a function of H in LaSb. The two temperature scales merge at $H_{\text{onset}} \simeq 0.4$ T and diverge with increasing field giving rise to a triangle. In the triangular region, $\rho(T)$ shows field-induced activation. The silver region above the triangle is where $\rho(T)$ behaves like a metal. The gold region below the triangle is where $\rho(T)$ plateaus. (b) Similar triangular phase diagram for LaBi. (c) Activation energy E_a extracted from the Arrhenius analysis in the shaded triangular region and plotted as a function of magnetic field for LaSb. (d) E_a plotted as a function of field for LaBi with a behavior comparable to LaSb.

conducting behavior is replaced with the plateau. T_m and T_i merge at H_{onset} and diverge as the field is increased. In section IV we show that a similar phase diagram can be constructed from the existing data in several transition-metal-based TSMs.

C. Field dependence of resistivity and extreme magnetoresistance

Figs. 4(a) and 4(b) show magnetoresistance, $\text{MR} = 100 \times [R(H) - R(0)]/R(0)$, as a function of magnetic field from $H = 0$ to 9 T at several temperatures. The black and the yellow curves at $T = 2$ K and 5 K superimpose since both curves are in the plateau region where MR reaches its *extreme* limit in excess of $10^5\%$. Comparing Figs. 4(a,b) with the phase diagram Figs. 3(a,b) shows that MR is small in the bulk metallic phase at $T > T_m$, it starts to increase in the semiconducting phase at $T_m > T > T_i$, and reaches the extreme limit in the plateau region at $T < T_i$. Ref. [22] shows that the magnitude of XMR is sensitive to the residual resistivity ratio RRR *i.e.* to the sample quality. We quote RRR val-

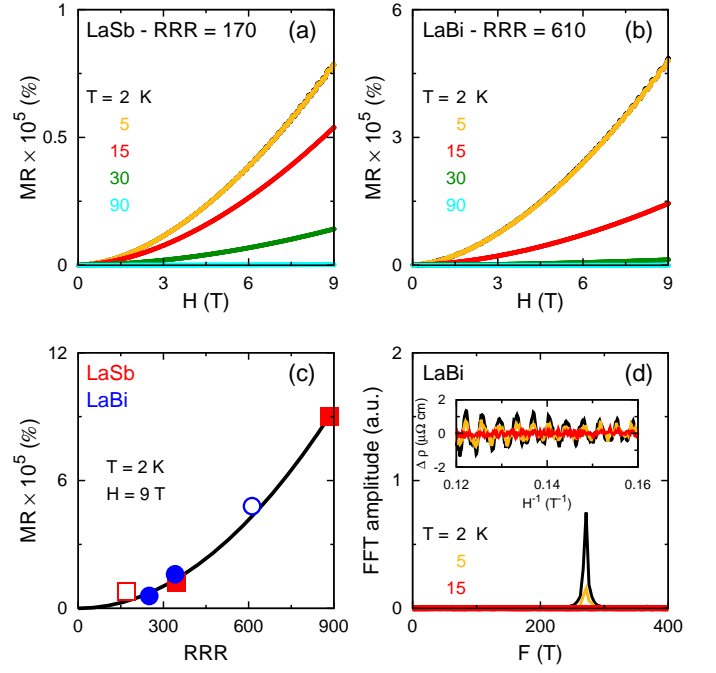


FIG. 4. (a) Magnetoresistance as a function of field in LaSb sample with RRR = 170 at several temperatures indicated on the figure. SdH oscillations appear at higher fields. (b) MR as a function of field for LaBi sample with RRR = 610. (c) MR at $T = 2$ K and $H = 9$ T plotted as a function of RRR for several LaSb (square) and LaBi (circle) samples from this work and Ref. [22]. Empty symbols mark the two samples studied here in detail. (d) Inset shows the oscillatory part of resistivity, $\Delta\rho(H^{-1})$, at several temperatures for LaBi. Fast Fourier Transform (FFT) of these data are plotted as a function of frequency with a peak at $F_0 = 217$ T.

ues for the LaSb and the LaBi samples in Fig. 4(a) and 4(b) to prevent the illusion that XMR in LaSb is smaller than LaBi. Fig. 4(c) is a plot of MR as a function of RRR for several LaSb and LaBi specimens with different RRR values. Empty symbols mark the two samples presented in this work. MR in both materials follows the same quadratic dependence on RRR showing a comparable XMR in both compounds given comparable sample quality. A similar quadratic dependence of XMR on RRR is reported in the flux-grown WTe_2 samples [13].

The ripples at higher fields in Figs. 4(a) and 4(b) are Shubnikov-de Haas (SdH) oscillations. The purely oscillatory part of resistivity $\Delta\rho(H)$ is obtained by subtracting a smooth H^2 background from $\rho(H)$. $\Delta\rho$ is periodic in H^{-1} as seen in the inset of Fig. 4(d). Fast Fourier Transform (FFT) of these data gives a peak at $F_0 = 271 \pm 5$ T in Fig. 4(d) for LaBi. Similar analysis gives $F_0 = 212 \pm 5$ T for LaSb [22]. The principal frequencies for LaSb and LaBi do not match the known frequencies of tin and indium ruling out flux inclusion [27, 28].

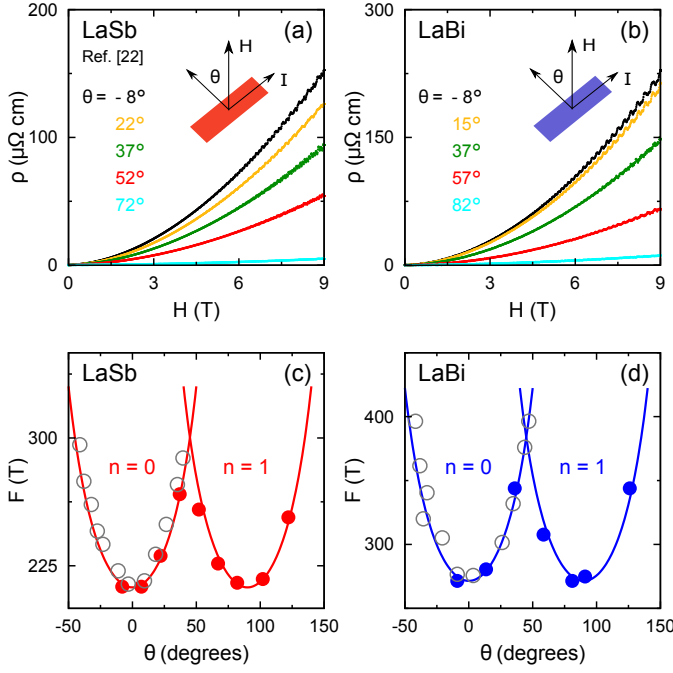


FIG. 5. (a) Resistivity as a function of magnetic field in LaSb at five representative angles as indicated. MR decreases with increasing θ . Shubnikov - de Haas (SdH) frequencies vary non-monotonically with θ . LaSb data are adapted from Ref. [22]. (b) $\rho(H)$ in LaBi at five representative angles as indicated. MR stays positive at all angles in both systems. (c) SdH frequency as a function of angle in LaSb. Empty gray circles are de Haas-van Alphen (dHvA) data from Ref. [29] limited to lower angles. Solid lines are fits to Eq. 1 with $F_0 = 212$ T. (d) SdH oscillation frequency as a function of angle in LaBi. Solid lines are fits to Eq. 1 with $F_0 = 271$ T. Empty gray symbols are dHvA data from Ref. [30].

D. Angle dependence of XMR and SdH oscillations

Figs. 5(a) and 5(b) show the angle dependence of XMR in LaSb and LaBi. The direction of magnetic field H and electrical current I with respect to $[100]$ crystal plane are shown schematically. XMR is maximum when $H \perp I$ and minimum when $H \parallel I$. It remains positive at all angles. Figs. 5(c) and 5(d) show that the principal frequency in LaSb and LaBi follows the angle dependence of a two dimensional Fermi surface:

$$F = \frac{F_0}{\cos\left(\theta - \frac{n\pi}{2}\right)} \quad (1)$$

where n is an integer, θ is the angle, and F_0 is the principal frequency at $\theta = 0$. These data show that the main frequencies at $F_0 = 212$ T in LaSb and $F_0 = 271$ T in LaBi belong to quasi-2D Fermi surfaces. Fig. 5(c) shows a good agreement between our data and prior studies of magnetic oscillations (gray symbols) [29–32]. Similar angle dependence of quantum oscillations in topological insulators has been taken as evidence for strictly 2D surface states of TIs [23, 33, 34]. SdH frequencies of LaSb

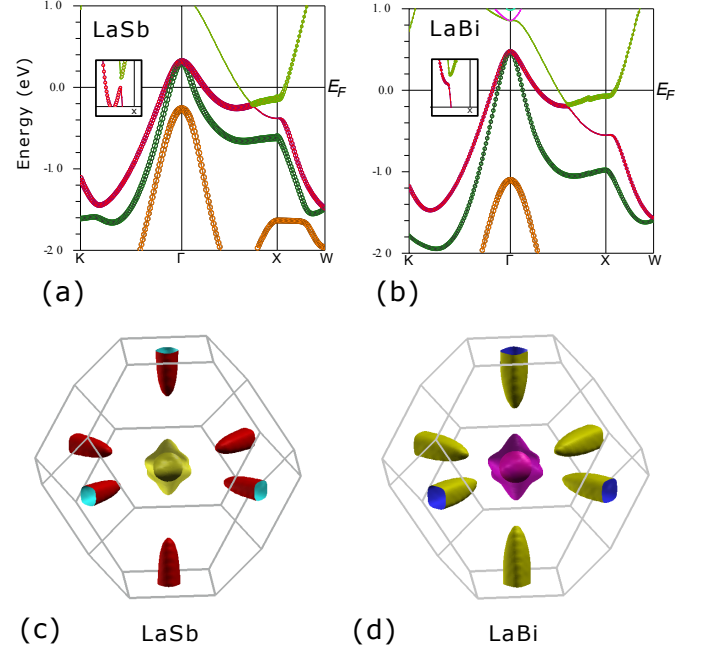


FIG. 6. (a) Band structure of LaSb with two hole pockets that cross E_F near Γ and one electron pocket that crosses E_F near X . The crossing between lanthanum d -states (thin bands) and Antimony p -states (thick bands) near X gives a d - p texture to the electron pocket due to spin-orbit coupling. The inset shows a small gap at this crossing. (b) Band structure of LaBi with the same d - p crossing between La thin bands and Bi thick bands near X . (c) Fermi surfaces of LaSb visualized in the first Brillouin zone with the central 3D hole pockets and the peripheral quasi-2D electron pockets. SdH frequencies in Fig. 5 correspond to these quasi-2D electron pockets. (d) Similar Fermi surfaces for LaBi.

and LaBi shown in Fig. 5 come from quasi-2D bulk states and not from strictly 2D surface states (section III E). As pointed out in Ref. [22], the combination of 2D or quasi-2D Fermiology and band inversion gives rise to analogous transport phenomenology in TIs and TSMs.

E. Band structure and the orbital texture of the quasi-2D Fermi surface

Figs. 6(a) and 6(b) show the results of our band structure calculations on LaSb and LaBi using the WIEN2k code [35]. In both systems, two hole bands at the Γ -point and one electron band near the X -point cross E_F . Figs. 6(c) and 6(d) visualize the corresponding Fermi surfaces with the two hole surfaces at the center of the Brillouin zone and the quasi-2D electron pockets crossing the faces. Prior studies of quantum oscillations in the magnetic and acoustic channels have detected these hole and electron Fermi surfaces in both materials [29–32]. The principal SdH frequencies that we observe in LaSb ($F_0 = 212$ T) and LaBi ($F_0 = 271$ T) match the cross-sectional area of

the quasi-2D surface at the X-point. Therefore, electrical transport in the plateau region of these materials is dominated by the quasi-2D electron pocket.

We plot Antimony p -states as thick bands and lanthanum d -states as thin bands in Figs. 6(a) and 6(b). These states cross near the X-point and form the quasi-2D electron pocket with a mixed d - p orbital texture. The inset in both Figures show a small gap at the crossing point driven by strong spin-orbit coupling similar to topological insulators. Therefore, the quasi-2D pocket that dominates the low temperature transport could acquire topological protection against scattering similar to the surface states of TIs. A magnetic field could interfere with the d - p orbital mixing and activate strong scattering on these pockets giving rise to XMR. Recent observations of circular dichroism by ARPES confirms the same orbital mixing in WTe₂ [36]. In Appendix B we show that the band structure of WTe₂ and several other topological semimetals have the same orbital texture as lanthanum monpnictides (Fig. 11). In section IV, we show that these other TSMs also have the same triangular phase diagram as lanthanum monpnictides. These observations strongly suggest that XMR in various TSMs is a result of orbital texture on quasi-2D Fermi surfaces.

F. Effective mass and Dingle temperature

Using the Onsager relation, we extract the Fermi wave vector and the density of carriers on the quasi-2D electron pocket from the frequency of SdH oscillations:

$$F = \frac{\phi_0}{2\pi^2} A_{\text{ext}}, \quad A_{\text{ext}} = \pi k_F^2, \quad k_F = (4\pi n_{2D})^{1/2} \quad (2)$$

where ϕ_0 , A_{ext} , k_F , and n_{2D} are the quantum of flux, the extremal orbit area, the Fermi wave vector, and the two dimensional carrier density for spin filtered electrons. Fig. 4(d) shows $F = 271$ T in LaBi, therefore, $k_F = 9.1 \times 10^6 \text{ cm}^{-1}$ and $n_{2D} = 6.6 \times 10^{12} \text{ cm}^{-2}$. Corresponding values for LaSb are given in Table I. The oscillation amplitude damps with increasing temperature and with decreasing magnetic field (Fig. 4(d)) according to:

$$\Delta\rho = R_L R_D \sin\left(\frac{2\pi F}{H} + \phi\right) \quad (3)$$

R_L is the Lifshitz-Kosevich factor that captures damping with increasing temperature:

$$R_L = \frac{X}{\sinh(X)}, \quad X = \frac{\alpha T m^*}{H} \quad (4)$$

where $\alpha = 2\pi^2 k_B m_e / e\hbar$ is a constant made of Boltzmann factor k_B , bare electron mass m_e , electron charge e , and reduced Plank constant \hbar . m^* is the effective electron mass in units of m_e . R_D is the Dingle factor that captures damping with decreasing field:

$$R_D = \exp(-X_D), \quad X_D = \frac{\alpha T_D m^*}{H} \quad (5)$$

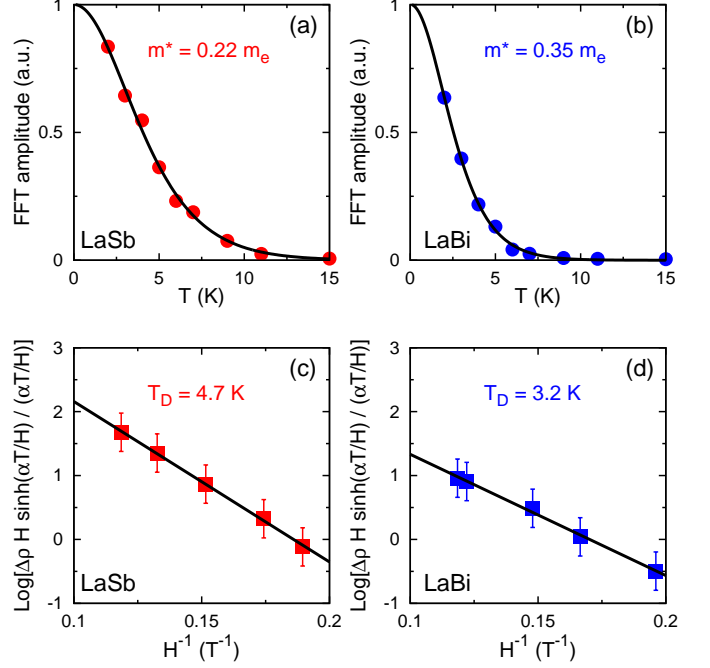


FIG. 7. (a) Amplitude of the Fast Fourier transform (FFT) of SdH oscillations with $F_0 = 212$ T plotted as a function of temperature for LaSb. Solid line is a fit to the Lifshitz-Kosevich formula (Eq. 4). The effective mass of carriers is extracted from the fit and reported on the figure. (b) Lifshitz-Kosevich analysis for LaBi. Effective mass in LaBi is slightly larger than LaSb. (c) FFT amplitudes modulated by the Lifshitz-Kosevich factor plotted as a function of H^{-1} for LaSb. Solid line is a fit to the Dingle formula (Eq. 5). Dingle temperature T_D is reported on the figure. (d) Dingle analysis for LaBi.

where T_D is the Dingle temperature from which the relaxation rate τ , the mean free path ℓ , and the mobility μ of charge carriers can be determined using:

$$k_B T_D = \frac{\hbar}{2\pi\tau}, \quad \ell = v_F \tau, \quad \mu = \frac{e\tau}{m^*} \quad (6)$$

with the Fermi velocity $v_F = \hbar k_F / m^*$.

Figs. 7(a) and 7(b) show the Lifshitz-Kosevich fit (Eq. 4) to the temperature dependence of the oscillation amplitude. The resulting effective masses are $m^* = 0.22 m_e$ for LaSb and $m^* = 0.35 m_e$ for LaBi. Figs. 7(c) and 7(d) show the Dingle fit (Eq. 5) to the field dependence of the oscillation amplitude that determines τ , ℓ , and μ for the carriers in the plateau region of LaSb and LaBi. Table I summarizes all the parameters from SdH oscillations and compares them to the corresponding values in the topological insulator Bi₂Te₂Se [23].

G. Hall effect and the two band model

Fig. 8(a) shows temperature dependence of the Hall coefficient $R_H = \rho_{xy}/H$ at $H = 9$ T in LaSb (red) and

TABLE I. Fermi surface parameters are tabulated for LaSb, LaBi, and Bi₂Te₂Se from the analysis explained in section III F (Eqs. 2 to 6). Data for Bi₂Te₂Se are adapted from Ref. [23].

Material	F [T]	m^*/m_e	T_D [K]	k_F [cm ⁻¹]	n_{2D} [cm ⁻²]	v_F [cm s ⁻¹]	τ [s]	ℓ [nm]	μ_e [cm ² V ⁻¹ s ⁻¹]
LaSb	212	0.22	7.8	8.0×10^6	5.1×10^{12}	4.2×10^7	1.6×10^{-13}	66	1250
LaBi	271	0.35	3.7	9.1×10^6	6.6×10^{12}	3.0×10^7	3.3×10^{-13}	98	1650
Bi ₂ Te ₂ Se	64	0.1	25.5	4.4×10^6	1.5×10^{12}	4.6×10^7	4.8×10^{-14}	22	760

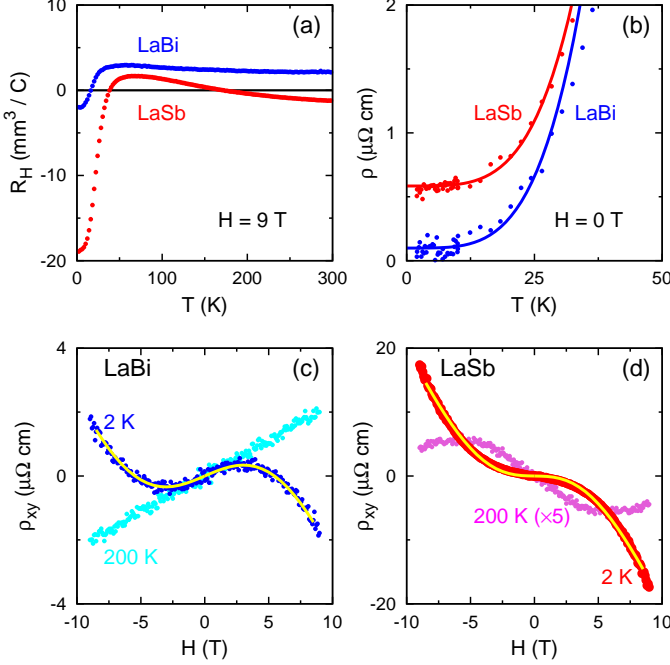


FIG. 8. (a) R_H at $H = 9$ T plotted as a function of temperature from $T = 2$ to 300 K in LaSb (red) and LaBi (blue). There is one sign change in LaBi at $T \simeq 20$ K and two sign changes in LaSb at $T \simeq 40$ K and 170 K. (b) $\rho(T)$ at $H = 0$ T and $T < 40$ K in LaSb and LaBi. Solid lines are fits of the form $\rho = \rho_0 + AT^4$ to determine $\rho_0 = 0.6 \mu\Omega\text{cm}$ in LaSb and $0.1 \mu\Omega\text{cm}$ in LaBi. (c) ρ_{xy} plotted as a function of field in LaBi from $H = -9$ to 9 T. The blue curve at $T = 2$ K fits to the two band model Eq. 7 (solid yellow line). The cyan curve at $T = 200$ K has a linear H dependence. (d) ρ_{xy} plotted as a function of field in LaSb from $H = -9$ to 9 T. The red curve at $T = 2$ K fits to the two band model Eq. 7 (solid yellow line). The magenta curve at $T = 200$ K remains non-linear in H . It is five times magnified for better visibility.

LaBi (blue). LaBi shows a clear two band behavior with positive R_H above $T \simeq 20$ K and negative R_H of comparable magnitude below $T \simeq 20$ K. LaSb shows a strong negative R_H signal below $T \simeq 40$ K and a weak positive signal above $T \simeq 40$ K that undergoes a second sign change at $T \simeq 170$ K. Fig. 8(b) shows power law fits to the resistivity data at low temperatures from which we extract residual resistivity $\rho_0 = 0.1 \mu\Omega\text{cm}$ in LaBi and $\rho_0 = 0.6 \mu\Omega\text{cm}$ in LaSb. Using the $T = 0$ limit of R_H from Fig. 8(a) and ρ_0 from Fig. 8(b) we can

estimate the transport mobility from the single band expression $\mu = R_H/\rho_0 = 3.2 \times 10^4 \text{ cm}^2\text{V}^{-1}\text{s}^{-1}$ in LaSb and $\mu = 2.5 \times 10^4 \text{ cm}^2\text{V}^{-1}\text{s}^{-1}$ in LaBi. Single band estimates for TSMs need to be taken with caution due to their multi-band nature. Note that these values are an order of magnitude larger than the more accurate values from quantum oscillations (table I).

Figs. 8(c) and 8(d) show the multiband behavior in the field dependence of the Hall resistivity ρ_{xy} in LaBi and LaSb. Solid yellow lines in both figures are fits to the two band expression for ρ_{xy} at $T = 2$ K [37, 38]:

$$\rho_{xy} = \frac{H}{e} \frac{(n_h\mu_h^2 - n_e\mu_e^2) + (n_h - n_e)(\mu_h\mu_e)^2 H^2}{(n_h\mu_h + n_e\mu_e)^2 + (n_h - n_e)^2(\mu_h\mu_e)^2 H^2} \quad (7)$$

where $n_{e/h}$ and $\mu_{e/h}$ are the electron/hole carrier density and mobility. Since the electron carriers at low temperatures come from the quasi-2D Fermi surfaces, we use the values in table I for μ_e and use $n_e = n^{2D}/d$ to calculate the effective 3D electron density where d is the inter-layer spacing. The fit gives an estimate for the hole carrier concentration n_h and mobility μ_h which we summarize in table II. The concentration of the hole carriers in LaBi agrees with a rough estimate using the single band formula $n_H = 1/eR_H = 3.1 \times 10^{21} \text{ cm}^{-3}$ using $R_H = 2 \text{ mm}^3\text{C}^{-1}$ from Fig. 8(a). This single band estimate in LaBi at high temperatures is justified by the linear field dependence of ρ_{xy} at $T = 200$ K as seen in Fig. 8(c). On the contrary, ρ_{xy} in LaSb remains nonlinear at high temperatures as seen in Fig. 8(d) which explains the second sign change at $T \simeq 170$ K in Fig. 8(a).

These results show that the details of electron-hole compensation is different between LaSb and LaBi, however, Fig. 4(c) suggests that XMR has comparable magnitude in both systems. Having electron-hole compensation is necessary for large MR as shown in Silver dichalcogenides [39, 40] but the detailed degree of compensation does not determine the magnitude of XMR in TSMs. Our hypothesis is that the orbital texture on the electron band plays the key role in determining the magnitude of XMR in topological semimetals. Comparing the mobility of hole pockets from Table II with electron pockets from table I shows that μ_h is an order of magnitude smaller than μ_e proving that the quasi-2D electron pockets indeed dominate electrical transport at low temperatures where XMR appears.

TABLE II. The hole carrier density n_h and mobility μ_h from the two band fit (Eq. 7) are listed for LaSb and LaBi.

Material	n_h [cm ⁻³]	μ_h [cm ² V ⁻¹ s ⁻¹]
LaSb	7.0×10^{20}	650
LaBi	2.7×10^{20}	780

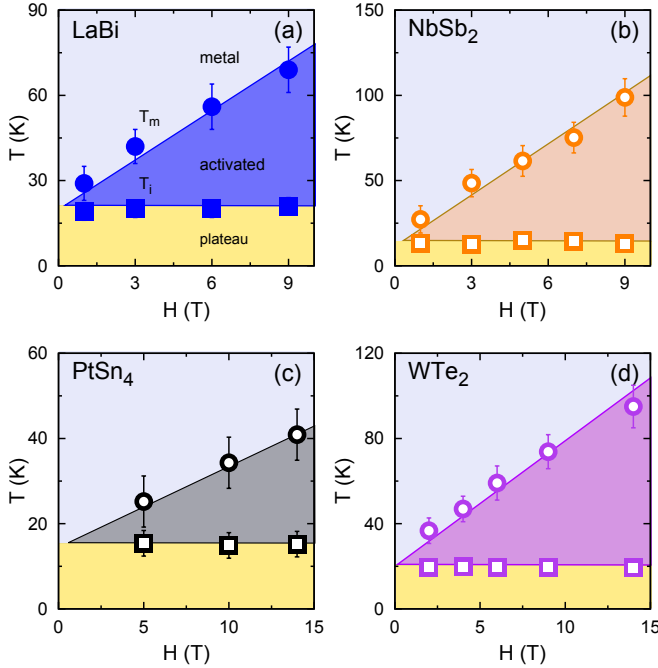


FIG. 9. (a) Triangular T - H phase diagram of LaBi, same as in Fig. 3(a), compared to three different topological semimetals in the subsequent panels. (b) Triangular T - H phase diagram in NbSb₂ constructed with the data from Ref. [15]. T_m (circles) and T_i (squares) are the temperatures of resistivity minimum and inflection as explained in section III A. Empty symbols are used for all the adapted data. (c) Triangular T - H phase diagram in PtSn₄ constructed with the data from Ref. [16]. (d) Triangular T - H phase diagram in WTe₂ constructed with the data from Ref. [12]. Aside from variations in the absolute values of T_m and T_i which depend on sample purity and XRM magnitude, these different topological semimetals share the same phase diagram.

IV. TRIANGULAR PHASE DIAGRAM IN TOPOLOGICAL SEMIMETALS

Our results in LaSb and LaBi can be summarized as below.

- (1) $\rho(T)$ at zero field shows a nearly perfect metal with very small ρ_0 (Fig. 2).
- (2) $\rho(T)$ in field shows a particular profile with a field-induced activation at T_m and a plateau below T_i (Fig. 2).
- (3) The field dependence of T_m and T_i constructs a triangular phase diagram where T_m and T_i diverge with increasing field and converge with decreasing field (Fig.

3).

(4) The field-induced activation of resistivity results in extreme magnetoresistance (XMR) that correlates with RRR (Fig. 4).

(5) The angle dependence of SdH oscillations shows that quasi-2D Fermi surfaces dominate electrical transport at low temperatures (Fig. 5).

(6) From the band structure, these quasi-2D surfaces have a mixed d - p orbital texture due to spin-orbit coupling (Fig. 6). XMR is possibly the consequence of disturbing such orbital texture by a magnetic field.

(7) The temperature and the field dependence of Hall effect show multi-band characteristics. A better electron-hole compensation is observed in LaBi compared to LaSb (Fig. 8), however, XMR is comparable between the two compounds as shown in Fig. 4(c).

These results suggest that XMR in LaSb and LaBi originate from the mixed orbital texture of their quasi-2D Fermi surfaces. In Appendix B we show that a similar orbital texture exists in the Fermiology of other topological semimetals with XMR including NbSb₂, PtSn₄, and WTe₂ (Fig. 11). The $\rho(T)$ and $\rho(H)$ profiles of these seemingly different materials are quite similar with a resistivity minimum at T_m and inflection at T_i . From the existing transport data in NbSb₂ [15], PtSn₄ [16], and WTe₂ [12], we extract T_m and T_i , construct their T - H phase diagrams, and compare to the triangular phase diagram of LaBi in Fig. 9. Remarkably, the same triangular phase diagram is observed despite the chemical and structural differences of these materials. Figs. 9 and 11 provide compelling evidence to identify orbital mixing on quasi-2D Fermi surfaces as the origin of XMR in TSMs.

ACKNOWLEDGMENTS

We thank S. R. Julian, and L. Muechler for helpful discussions. This research was supported by the Gordon and Betty Moore Foundation under the EPiQS program, grant GBMF 4412. S.K.K is supported by the ARO MURI on topological insulators, grant W911NF-12-1-0461.

Appendix A: Characterization of LaSb and LaBi samples with XRD

Fig 10(a) and 10(b) show powder x-ray diffraction patterns of our LaSb and LaBi samples. XRD data were acquired in a Bruker D8 ADVANCE ECO system with LYNXEYE XE high resolution energy-dispersive 1D detector. Rietveld refinement of these patterns are shown as solid black lines in Fig. 10. Refinements were done through the Fullprof software [41] using Thompson-Cox-Hastings pseudo Voigt profile convoluted with axial divergence asymmetry.

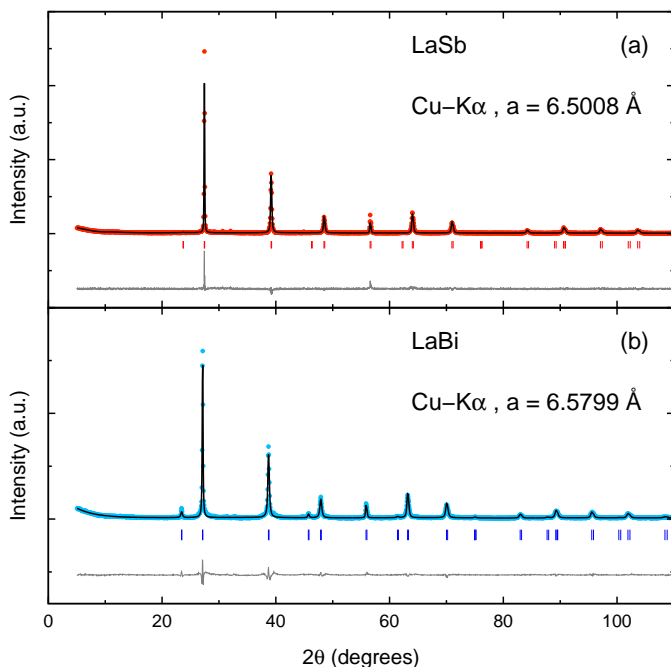


FIG. 10. (a) Rietveld refinement (solid black line) on powder XRD pattern (red circles) for LaSb. Lattice parameter from the refinement is quoted on the figure. (b) Rietveld refinement (solid black line) on powder XRD pattern (blue circles) for LaBi.

Appendix B: DFT calculations on NbSb₂, PtSn₄, and WTe₂

Fig. 11 shows the results of our density functional theory (DFT) calculations using WIEN2k code [35] on LaBi, NbSb₂, PtSn₄, and WTe₂. Regions of mixed *d-p* orbital texture due to spin-orbit coupling are marked with blue circles. All these semimetals have quasi-2D Fermi surfaces similar to Fig. 6(c) and 6(d) for LaSb and LaBi [12, 15, 16]. Extreme magnetoresistance in these materials has the same triangular phase diagram as in lanthanum monopnictides (Fig. 9). Similar phase diagram (Fig. 9) and similar band structure (Fig. 11) in these materials point towards a common origin for XMR in TSMs as discussed in section IV.

* ftafti@princeton.edu

- [1] J. M. Daughton, Journal of Magnetism and Magnetic Materials **192**, 334 (1999).
- [2] C. N. R. Rao and A. K. Cheetham, Science **272**, 369 (1996).
- [3] S. A. Wolf, D. D. Awschalom, R. A. Buhrman, J. M. Daughton, S. v. Molnr, M. L. Roukes, A. Y. Chtchelkanova, and D. M. Treger, Science **294**, 1488 (2001).
- [4] J. Lenz, Proceedings of the IEEE **78**, 973 (1990).
- [5] J. Jankowski, S. El-Ahmar, and M. Oszwaldowski, Sensors (Basel, Switzerland) **11**, 876 (2011).
- [6] A. P. Ramirez, Journal of Physics: Condensed Matter **9**, 8171 (1997).
- [7] J. Xiong, S. K. Kushwaha, T. Liang, J. W. Krizan, M. Hirschberger, W. Wang, R. J. Cava, and N. P. Ong, Science **350**, 413 (2015).
- [8] T. Liang, Q. Gibson, M. N. Ali, M. Liu, R. J. Cava, and N. P. Ong, Nature Materials **14**, 280 (2015).
- [9] C. Shekhar, A. K. Nayak, Y. Sun, M. Schmidt, M. Nicklas, I. Leermakers, U. Zeitler, Y. Skourski, J. Wosnitza, Z. Liu, Y. Chen, W. Schnelle, H. Borrmann, Y. Grin, C. Felser, and B. Yan, Nature Physics **11**, 645 (2015).
- [10] N. J. Ghimire, Y. Luo, M. Neupane, D. J. Williams, E. D. Bauer, and F. Ronning, Journal of Physics: Condensed Matter **27**, 152201 (2015).
- [11] X. Huang, L. Zhao, Y. Long, P. Wang, D. Chen, Z. Yang, H. Liang, M. Xue, H. Weng, Z. Fang, X. Dai, and G. Chen, Physical Review X **5**, 031023 (2015).
- [12] M. N. Ali, J. Xiong, S. Flynn, J. Tao, Q. D. Gibson, L. M. Schoop, T. Liang, N. Haldolaarachchige, M. Hirschberger, N. P. Ong, and R. J. Cava, Nature **514**, 205 (2014).
- [13] M. N. Ali, L. Schoop, J. Xiong, S. Flynn, Q. Gibson, M. Hirschberger, N. P. Ong, and R. J. Cava, EPL (Europhysics Letters) **110**, 67002 (2015).
- [14] Z. Zhu, X. Lin, J. Liu, B. Fauque, Q. Tao, C. Yang, Y. Shi, and K. Behnia, Physical Review Letters **114**, 176601 (2015).
- [15] K. Wang, D. Graf, L. Li, L. Wang, and C. Petrovic, Scientific Reports **4** (2014).
- [16] E. Mun, H. Ko, G. J. Miller, G. D. Samolyuk, S. L. Bud'ko, and P. C. Canfield, Physical Review B **85**, 035135 (2012).
- [17] S. Borisenko, Q. Gibson, D. Evtushinsky, V. Zabolotnyy, B. Buchner, and R. J. Cava, Physical Review Letters **113**, 027603 (2014).
- [18] H. Weng, C. Fang, Z. Fang, B. A. Bernevig, and X. Dai, Physical Review X **5**, 011029 (2015).
- [19] S.-Y. Xu, N. Alidoust, I. Belopolski, Z. Yuan, G. Bian, T.-R. Chang, H. Zheng, V. N. Strocov, D. S. Sanchez, G. Chang, C. Zhang, D. Mou, Y. Wu, L. Huang, C.-C. Lee, S.-M. Huang, B. Wang, A. Bansil, H.-T. Jeng, T. Neupert, A. Kaminski, H. Lin, S. Jia, and M. Zahid Hasan, Nature Physics **11**, 748 (2015).
- [20] I. Pletikoscic, M. N. Ali, A. Fedorov, R. Cava, and T. Valla, Physical Review Letters **113**, 216601 (2014).

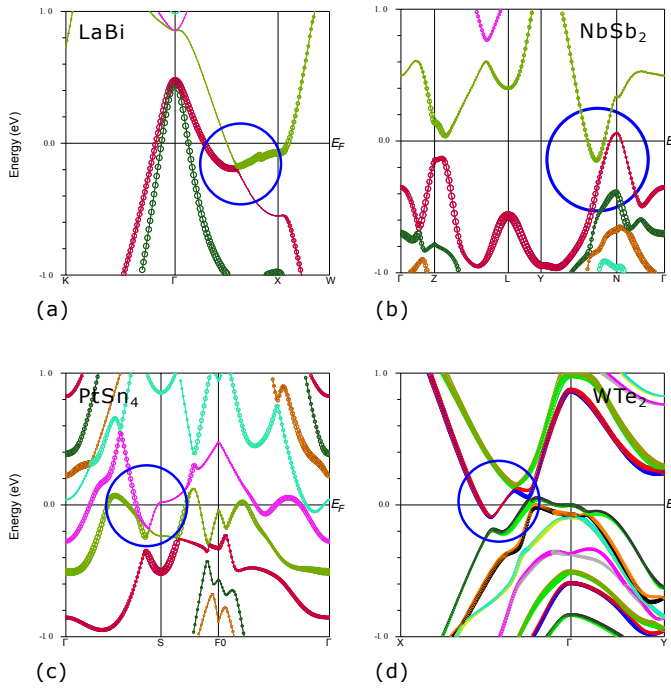


FIG. 11. (a) Band structure of LaBi, same as in Fig. 6(b). The blue circle marks the region of d - p orbital mixing. (b) Band structure of NbSb₂ with a similar d - p mixing inside the blue circle. (c) Band structure of PtSn₄ with similar d - p mixing. (d) Band structure of WTe₂ with similar d - p mixing.

- [21] M. Zeng, C. Fang, G. Chang, Y.-A. Chen, T. Hsieh, A. Bansil, H. Lin, and L. Fu, arXiv:1504.03492 [cond-mat] (2015).
- [22] F. F. Tafti, Q. D. Gibson, S. K. Kushwaha, N. Hal-dolaarachchige, and R. J. Cava, arXiv:1510.06931 [cond-mat] (2015).
- [23] Z. Ren, A. A. Taskin, S. Sasaki, K. Segawa, and Y. Ando, Physical Review B **82**, 241306 (2010).
- [24] S. Jia, H. Beidenkopf, I. Drozdov, M. K. Fuccillo, J. Seo, J. Xiong, N. P. Ong, A. Yazdani, and R. J. Cava, Physical Review B **86**, 165119 (2012).
- [25] D. J. Kim, S. Thomas, T. Grant, J. Botimer, Z. Fisk, and J. Xia, Scientific Reports **3** (2013).
- [26] D. J. Kim, J. Xia, and Z. Fisk, Nature Materials **13**, 466 (2014).
- [27] J. M. Deacon and L. Mackinnon, Journal of Physics F: Metal Physics **3**, 2082 (1973).
- [28] J. E. Cowey, R. Gerber, and L. Mackinnon, Journal of Physics F: Metal Physics **4**, 39 (1974).
- [29] H. Kitazawa, T. Suzuki, M. Sera, I. Oguro, A. Yanase, A. Hasegawa, and T. Kasuya, Journal of Magnetism and Magnetic Materials **31**, 421 (1983).
- [30] A. Hasegawa, Journal of the Physical Society of Japan **54**, 677 (1985).
- [31] R. Settai, T. Goto, S. Sakatsume, Y. S. Kwon, T. Suzuki, and T. Kasuya, Physica B: Condensed Matter **186**, 176 (1993).
- [32] M. Yoshida, K. Koyama, T. Tomimatsu, M. Shirakawa, A. Ochiai, and M. Motokawa, Journal of the Physical Society of Japan **70**, 2078 (2001).
- [33] G. Li, Z. Xiang, F. Yu, T. Asaba, B. Lawson, P. Cai, C. Tinsman, A. Berkley, S. Wolgast, Y. S. Eo, D.-J. Kim, C. Kurdak, J. W. Allen, K. Sun, X. H. Chen, Y. Y. Wang, Z. Fisk, and L. Li, Science **346**, 1208 (2014).
- [34] B. S. Tan, Y.-T. Hsu, B. Zeng, M. C. Hatnean, N. Harrison, Z. Zhu, M. Hartstein, M. Kiourlappou, A. Srivastava, M. D. Johannes, T. P. Murphy, J.-H. Park, L. Balicas, G. G. Lonzarich, G. Balakrishnan, and S. E. Sebastian, Science **349**, 287 (2015).
- [35] P. Blaha, K. Schwarz, G. Madsen, D. Kvasnicka, and J. Luitz, *WIEN2K, An Augmented Plane Wave + Local Orbitals Program for Calculating Crystal Properties* (Karlheinz Schwarz, Techn. Universitt Wien, Austria, Wien, Austria, 2001).
- [36] J. Jiang, F. Tang, X. Pan, H. Liu, X. Niu, Y. Wang, D. Xu, H. Yang, B. Xie, F. Song, P. Dudin, T. Kim, M. Hoesch, P. K. Das, I. Vobornik, X. Wan, and D. Feng, Physical Review Letters **115**, 166601 (2015).
- [37] H. Takahashi, R. Okazaki, Y. Yasui, and I. Terasaki, Physical Review B **84**, 205215 (2011).
- [38] B. Xia, P. Ren, A. Sulaev, P. Liu, S.-Q. Shen, and L. Wang, Physical Review B **87**, 085442 (2013).
- [39] R. Xu, A. Husmann, T. F. Rosenbaum, M.-L. Saboungi, J. E. Enderby, and P. B. Littlewood, Nature **390**, 57 (1997).
- [40] M. Lee, T. F. Rosenbaum, M.-L. Saboungi, and H. S. Schnyders, Physical Review Letters **88**, 066602 (2002).
- [41] J. Rodriguez-Carvajal, Physica B: Condensed Matter **192**, 55 (1993).